






The magnetic field on thermosolutal convection in an annulus between two super ellipses

Abdelraheem M. Aly ^{a,b}, Zehba Raizah ^a and Mohammad Ghalambaz ^{c,d}

^aDepartment of Mathematics, Faculty of Science, King Khalid University, Abha, Saudi Arabia; ^bDepartment of Mathematics, Faculty of Science, South Valley University, Qena, Egypt; ^cMetamaterials for Mechanical, Biomechanical and Multi physical Applications Research Group, Ton Duc Thang University, Ho Chi Minh City, Vietnam; ^dFaculty of Applied Sciences, Ton Duc Thang University, Ho Chi Minh City, Vietnam

ABSTRACT

The current study deals with the impacts of an inclined magnetic field on the double-diffusive convection of the nano-encapsulated phase change materials (NEPCM) suspended in an annulus between two super ellipses. A novel shape between two super ellipses having the positive numbers $n = 3/2$ and $a = b$. The controlling transformed equations are solved by employing the (ISPH) method. The heat/mass source with variable length is put on the left side of an annulus. Impacts of ($Ha = 0 - 40$), ($\gamma = 0^\circ - 90^\circ$), ($\theta_f = 0.05 - 0.95$), ($\varphi = 0.01 - 0.04$), ($L_x = 0.1 - 1$), ($Ste = 0.1 - 0.8$), and ($Ra = 10^3 - 10^5$) on the melting/solidification zone and heat/mass transfer performance are investigated. It was remarked that the melting/solidification zone shifts nearly to the heat/mass source according to a growing on Ha . The L_x induces an improvement of the heat/mass transmission and nanofluid movements within an annulus. Increasing the θ_f is working well in enhancing the melting/solidification zone and make it much closer to the heater within an annulus, and it boosts the nanofluid velocity by 4.24%. Increasing φ to 0.04 strengthens the melting/solidification zone and declines the nanofluid velocity by 14.68%. An augmentation in Ra powers the nanofluid speed, heat/mass transport, and melting/solidification zone within an annulus. Average \overline{Nu} , and average \overline{Sh} are decreasing as Ha and L_x are increased.

ARTICLE HISTORY

Received 21 December 2021
Accepted 7 June 2022

KEYWORDS

ISPH; superellipse; NEPCM; annulus; rhombus shape; nanofluid

Nomenclature

| | |
|-------|---|
| B_0 | magnetic field strength |
| C | dimensional concentration |
| C_p | specific heat, ($Jkg^{-1}K^{-1}$) |
| Cr | heat capacity |
| g | acceleration of gravity ($m\ s^{-2}$) |
| Ha | Hartmann number, $\left(B_0 L \sqrt{\frac{\sigma_f}{\mu_f}}\right)$ |
| k | thermal conductivity ($W\ m^{-1}\ K^{-1}$) |

| | |
|--------|---|
| L_e | Lewis number $\left(\frac{\nu_f}{D_{eff}}\right)$ |
| L_x | partial heat/mass source length (m) |
| N | buoyancy ratio parameter $\left(\frac{\beta_c(C_h - C_c)}{\beta_T(T_h - T_c)}\right)$ |
| Nu | Nusselt number |
| p | pressure (Pa) |
| Pr | Prandtl number, $\left(\frac{\nu_f}{\alpha_f}\right)$ |
| Ra | Rayleigh number, $\left(\frac{\beta_f g(T_h - T_c)L^3}{\alpha_f \nu_f}\right)$ |
| Sh | Sherwood number |
| t | dimensional time (s) |
| T | dimensional temperature (K) |
| U, V | dimensionless velocities |
| u, v | dimensional velocities ($m\ s^{-1}$) |
| X, Y | dimensionless Cartesian coordinates |
| x, y | dimensional Cartesian coordinates (m) |

Greek symbols

| | |
|---------------|--|
| α | thermal diffusivity ($m^2\ s^{-1}$) |
| Γ | Gamma function |
| ε | porosity |
| β | thermal expansion coefficient (K^{-1}) |
| δ | temperature parameter (K) |
| γ | a magnetic field inclination angle |
| ν | kinematic viscosity, (m^2s^{-1}) |
| θ | dimensionless temperature |
| φ | nanoparticle volume fraction |
| Φ | Dimensionless concentration |
| μ | dynamic viscosity ($kg\ m^{-1}\ s^{-1}$) |
| ρ | density ($kg\ m^{-3}$) |
| σ | electrical conductivity |
| τ | dimensionless time |

Subscripts

| | |
|-----|-----------------------------------|
| b | bulk properties of the suspension |
| C | cold |
| h | hot |
| f | fluid |
| p | nanoparticles |

1. Introduction

In the field of building heating or cooling systems, solar energy collectors, and electronic cooling, thermal energy storage plays an important role. Thermal devices with higher heat

transfer capabilities need to be developed to increase the thermal energy storage. The enhancement of the heat transfer with the traditional fluids is limited. In the last few years, the researchers discovered a new technique for using phase change materials for thermal control systems. The fluid which contains micro or nano-encapsulated particles of phase change material will play wide roles in the energy storage systems. A lot of theoretical and experimental studies were investigated to illustrate the effects of the nano-encapsulated phase change materials (NEPCM) on the heat transfer inside the different shapes of cavities [1–3].

The convection heat inside cavities with the partially heated wall is one of the interesting fields for applications such as glass melting, electronics cooling, and process engineering. Thus, it has taken the attention of the researchers. For example, Hamid et al. [4] and Khan et al. [5] reported the convection flow inside a partially heated trapezoidal cavity. Cho [6] presented a study on the partially heated wavy cavity. Ul Haq et al. [7] studied the effect of a partially heated wall of hexagon cavity. The partially heated wall of a square cavity was investigated by Nie et al. [8]. Aneja et al. [9], Abu-Hamdeh et al. [10]. They all showed that the heat transfer was affected by the length and the location of the heating source.

In fluids dynamics, double-diffusive convection occurs due to the different density gradients inside the fluid. These differences in the density usually caused by differences in temperature or when the fluid composition is gradients. The double-diffusion topics are one of the interesting fields for researchers because of their wide applications [11–17].

The popularization of the enhancement of heat and mass transfer has led to the diversification of studying different forms of cavities. More recently, numerous studies have examined the influence of the different geometry cavities shapes on the heat transfer performance. The reader can see the diversity of research in the many different shapes of the cavity such as V-shaped [18], H-shaped [19,20], L-shaped [21,22], hexagonal-shaped [7,23,24], Rhombus shaped [25,26], and so on.

The double-diffusive of NEPCMs suspended inside an annulus between two super ellipses using the ISPH method is the main objective of this study. The simulations were performed for various values of Hartmann number Ha , heat/mass source length L_x , solid volume fraction φ , a fusion temperature parameter θ_f , the inclination angle γ , Rayleigh number Ra , and the Stefan parameter Ste . It is observed that the average \overline{Nu} is enhanced according to an increment in φ and Ste , whilst it declines as Ha and L_x are raising. The melting/solidification zone shifts nearly to the heat/mass source according to a growing on the fusion temperature and Hartmann numbers.

2. Mathematical analysis

Figure 1 shows the geometry of the present problem. The source of the heater T_h and high concentration C_h is in the left side of an annulus with a variable length l_x and the other part of the left wall is adiabatic. The right and inner walls of an annulus are kept at cold T_c and low concentration C_c . The annulus is suspended by NEPCMs considering the influences of an inclined magnetic field. The attributes of the mixture fluid are presented in Table 1.

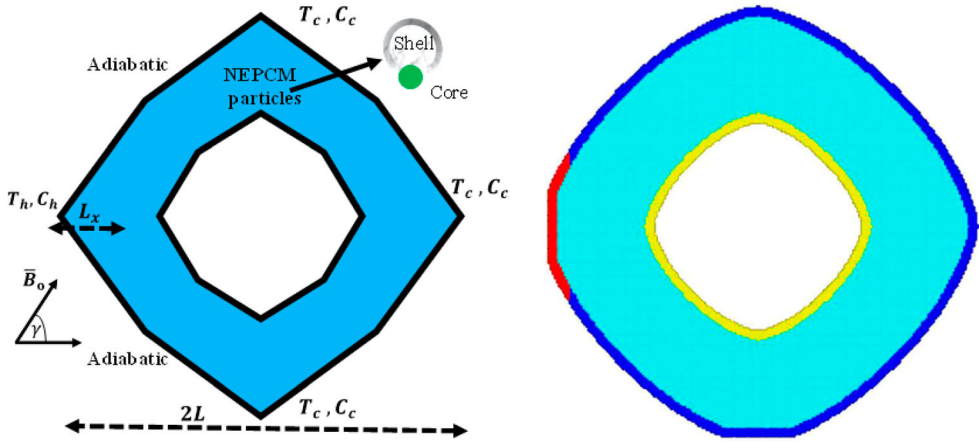


Figure 1. Geometry of the present problem.

Table 1. Attributes of the mixture fluid as [27].

| | Material | k | C_p | ρ | $\beta \times 10^{-5}$ |
|------------|--------------|-------|--------|--------|------------------------|
| Base fluid | Water [25°C] | 0.613 | 4179 | 997.1 | 21 |
| Core | Nonadecane | | 1317.7 | 786 | 17.28 |
| Shell | Polyurethane | | 2037 | 721 | |

The governing equations in a dimensionless form are:

$$\frac{\partial U}{\partial X} + \frac{\partial V}{\partial Y} = 0, \quad (1)$$

$$\frac{dU}{d\tau} = -\frac{\rho_f}{\rho_b} \frac{\partial P}{\partial X} + \frac{\mu_b}{\mu_f} \frac{\rho_f}{\rho_b} Pr \left(\frac{\partial^2 U}{\partial X^2} + \frac{\partial^2 U}{\partial Y^2} \right) - \frac{\sigma_b}{\sigma_f} \frac{\rho_f}{\rho_b} Pr Ha^2 (U \sin^2 \gamma - V \sin \gamma \cos \gamma), \quad (2)$$

$$\begin{aligned} \frac{dV}{d\tau} = & -\frac{\rho_f}{\rho_b} \frac{\partial P}{\partial Y} + \frac{\mu_b}{\mu_f} \frac{\rho_f}{\rho_b} Pr \left(\frac{\partial^2 V}{\partial X^2} + \frac{\partial^2 V}{\partial Y^2} \right) + \frac{(\rho\beta)_b}{(\rho\beta)_f} \frac{\rho_f}{\rho_b} Ra Pr (\theta + N\Phi) \\ & - \frac{\sigma_b}{\sigma_f} \frac{\rho_f}{\rho_b} Pr Ha^2 (V \cos^2 \gamma - U \sin \gamma \cos \gamma), \end{aligned} \quad (3)$$

$$Cr \frac{d\theta}{d\tau} = \frac{k_{m,b}}{k_f} \left[\frac{\partial^2 \theta}{\partial X^2} + \frac{\partial^2 \theta}{\partial Y^2} \right], \quad (4)$$

$$\frac{d\Phi}{d\tau} = \frac{1}{Le} \left[\frac{\partial^2 \Phi}{\partial X^2} + \frac{\partial^2 \Phi}{\partial Y^2} \right]. \quad (5)$$

$Pr = \frac{\nu_f}{\alpha_f}$ is the Prandtl number, $Ha = B_0 H \sqrt{\sigma_f / \mu_f}$ is the Hartmann number, and $Ra = \frac{\beta_f g (T_h - T_c) L^3}{\alpha_f \nu_f}$ is a Raleigh number. $Le = \frac{\nu_f}{D_{eff}}$ is a Lewis number.

The used dimensionless amounts:

$$X = \frac{x}{L}, Y = \frac{y}{L}, U = \frac{uL}{\alpha_f}, V = \frac{vL}{\alpha_f}, \theta = \frac{T - T_c}{T_h - T_c}, \Phi = \frac{C - C_c}{C_h - C_c}, P = \frac{pL^2}{\rho_f \alpha_f^2}, \tau = \frac{tL^2}{\alpha_f}, \quad (6)$$

The boundary conditions are:

$$\text{Right and inner walls : } U = V = 0, \theta = \Phi = 0, \quad (7a)$$

$$\text{Left wall : } U = V = 0, \frac{\partial \theta}{\partial \mathbf{n}} = \frac{\partial \Phi}{\partial \mathbf{n}} = 0, \quad (7b)$$

$$\text{Partial heater (left wall) : } U = V = 0, \theta = \Phi = 1, \quad (7c)$$

Nanofluid properties

Mixture density as [27] is:

$$\rho_b = \varphi \rho_p + \rho_f(1 - \varphi), \quad (8)$$

where ρ_p is calculated as:

$$\rho_p = \frac{(1 + \chi) \rho_s \rho_c}{\rho_s + \chi \rho_c} \quad (9)$$

where ρ_s and ρ_c are the density of a shell and core, respectively.

Specific heat capacity:

$$(C_p)_b = \frac{\varphi \rho_p (C_p)_p + \rho_f (C_p)_f - \varphi \rho_f (C_p)_f}{\rho_b}. \quad (10)$$

The heat capacity of encapsulated nanoparticles:

$$(C_p)_p = \frac{((C_p)_{c,l} + \chi (C_p)_s) \rho_s \rho_c}{(\rho_s + \chi \rho_c) \rho_p}. \quad (11)$$

In this study, the following sine profile is used:

$$(C_p)_c = (C_p)_{c,l} + \left[\frac{\pi}{2} \left(\frac{h_{sf}}{T_{Mr}} - (C_p)_{c,l} \right) \sin \left(\pi \frac{T - T_f + \frac{T_{Mr}}{2}}{T_{Mr}} \right) \right] \omega, \quad (12)$$

where,

$$\omega = \begin{cases} 0 & T < T_f - \frac{T_{Mr}}{2} \\ 1 & \left(T_f - \frac{T_{Mr}}{2} \right) < T < \left(T_f + \frac{T_{Mr}}{2} \right) \\ 0 & T > T_f + \frac{T_{Mr}}{2} \end{cases} \quad (13)$$

The thermal expansion:

$$\beta_b = \beta_f - \varphi \beta_f + \varphi \beta_p, \mu_b = \mu_f(1 + N_1 \varphi), k_b = k_f(1 + N_2 \varphi). \quad (14)$$

The dynamic viscosity:

$$\mu_b = \mu_f(1 + N_1 \varphi), \quad (15)$$

The thermal conductivity:

$$k_b = k_f(1 + N_2\varphi), \quad (16)$$

The electrical conductivity is:

$$\sigma_b = \sigma_f(1 + N_3\varphi), \quad (17)$$

where N_1 is dynamic viscosity number. N_2 is thermal conductivity number. N_3 is an electrical conductivity number. Their values are taken as $N_1 = 12.5$, $N_2 = 23.8$, and $N_3 = 3$.

The density ratio:

$$\frac{\rho_b}{\rho_f} = 1 - \varphi + \frac{\rho_p}{\rho_f}\varphi. \quad (18)$$

The thermal conductivity:

$$\frac{k_{m,b}}{k_f} = 1 + N_2\varphi. \quad (19)$$

The thermal expansion is:

$$\frac{\beta_b}{\beta_f} = 1 - \varphi + \frac{\beta_p}{\beta_f}\varphi. \quad (20)$$

The heat capacity:

$$Cr = \frac{(\rho C_p)_b}{(\rho C_p)_f} = 1 - \varphi + \lambda\varphi + \frac{\varphi}{\delta Ste} \left[\frac{\pi}{2} \Gamma \sin \left(\frac{\pi}{\delta} (\theta - \theta_f + \frac{\delta}{2}) \right) \right], \quad (21)$$

with

$$\Gamma = \begin{cases} 0 & \theta < \theta_f - \frac{\delta}{2} \\ 1 & (\theta_f - \frac{\delta}{2}) < \theta < (\theta_f + \frac{\delta}{2}), \\ 0 & \theta > \theta_f + \frac{\delta}{2} \end{cases} \quad (22)$$

where,

$$\theta_f = \frac{T_f - T_c}{\Delta T}, \quad \delta = \frac{T_{Mr}}{\Delta T}, \quad \lambda = \frac{((C_p)_{c,l} + \chi(C_p)_s)\rho_s \rho_c}{(\rho_s + \chi \rho_c)(\rho C_p)_f}, \quad Ste = \frac{(\rho C_p)_f \Delta T (\rho_s + \chi \rho_c)}{(1 + \chi) h_{sf} \rho_s \rho_c},$$

The average Sherwood number measured on the heat/mass source:

$$\overline{Sh} = \frac{-1}{L_h} \int_0^{L_h} \frac{\partial \Phi}{\partial \mathbf{n}} d\zeta, \quad (23)$$

The average Nusselt number measured on the heat/mass source:

$$\overline{Nu} = \frac{-1}{L_h} \int_0^{L_h} \frac{k_{m,b}}{k_f} \frac{\partial \theta}{\partial \mathbf{n}} d\zeta, \quad (24)$$

where L_h is the total length of the heat/mass source.

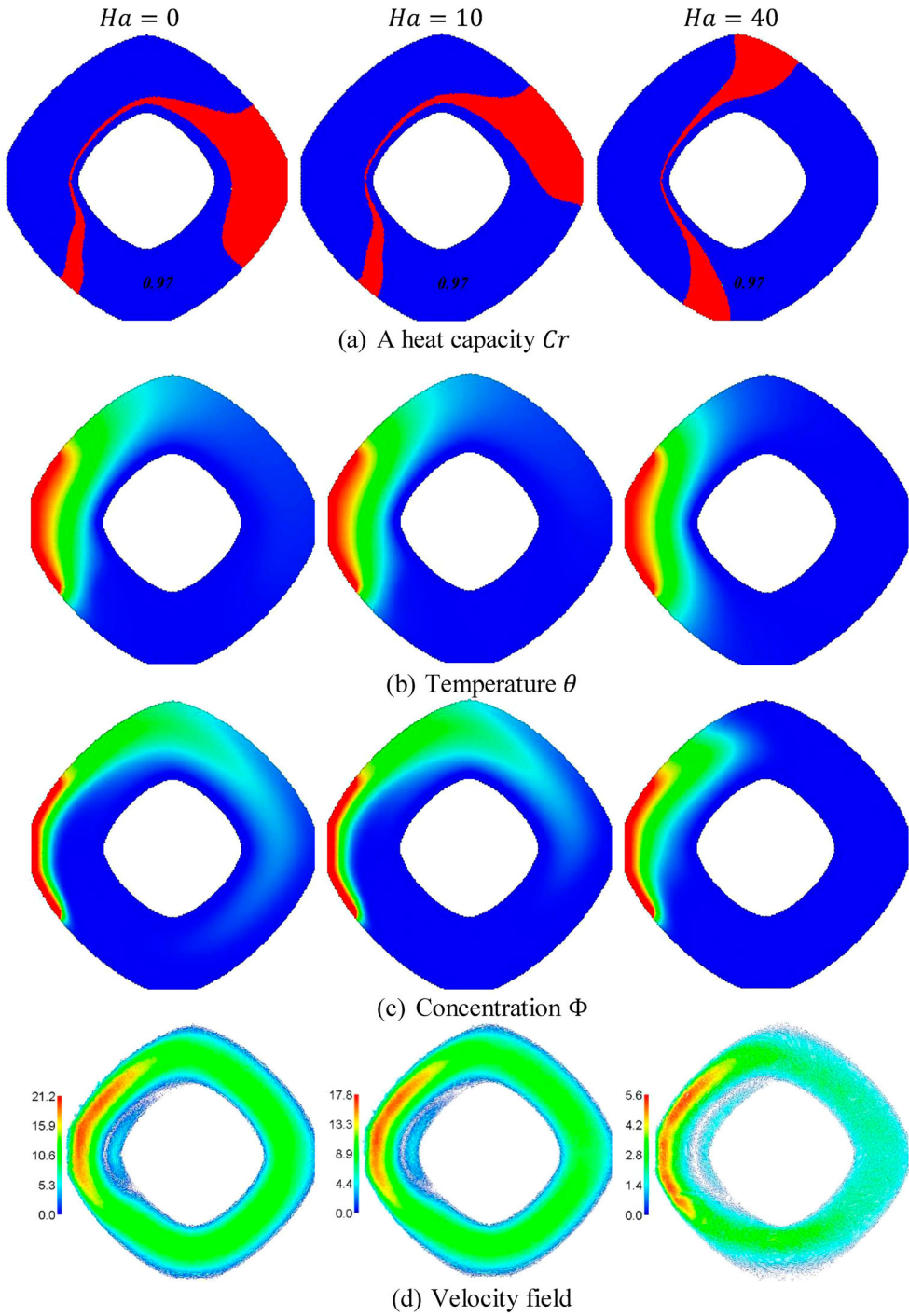


Figure 2. Effects of Hartmann number on the regulating fields at $\gamma = 30^\circ$, $\varphi = 0.05$, $\theta_f = 0.05$, $N = 1$, $Le = 10$, $L_x = 0.2$, $Ra = 10^4$, and $Ste = 0.2$.

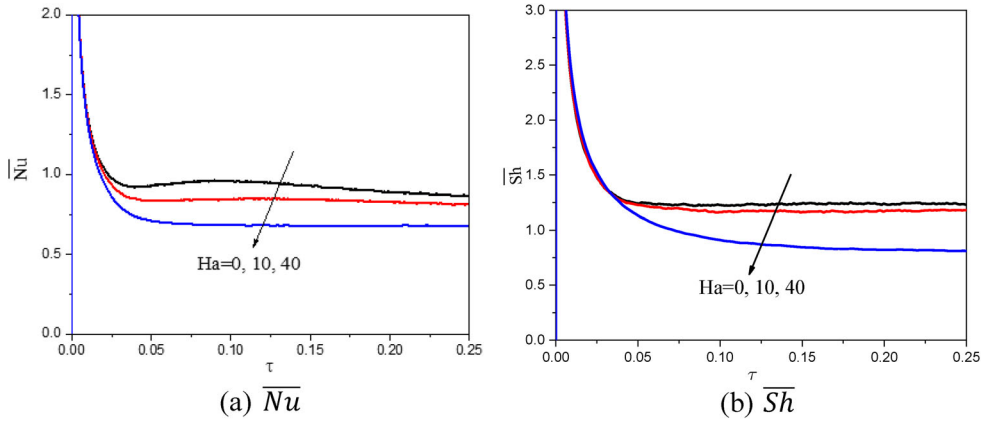


Figure 3. Effects of Hartmann number on \overline{Nu} and \overline{Sh} at $\gamma = 30^\circ$, $\varphi = 0.05$, $\theta_f = 0.05$, $N = 1$, $Le = 10$, $L_x = 0.2$, $Ra = 10^4$, and $Ste = 0.2$.

3. ISPH method

The solver steps of the ISPH method are:

Step 1:

$$U^* = \frac{\mu_b}{\mu_f} \frac{\rho_f \Delta \tau}{\rho_b} Pr \left(\frac{\partial^2 U}{\partial X^2} + \frac{\partial^2 U}{\partial Y^2} \right)^n - \frac{\Delta \tau \sigma_b \rho_f}{\sigma_f \rho_b} Ha^2 Pr (U^n \sin^2 \gamma - V^n \sin \gamma \cos \gamma) + U^n \quad (25)$$

$$V^* = \frac{\mu_b}{\mu_f} \frac{\rho_f \Delta \tau}{\rho_b} Pr \left(\frac{\partial^2 V}{\partial X^2} + \frac{\partial^2 V}{\partial Y^2} \right)^n + \frac{\Delta \tau \rho_f (\rho \beta)_b}{\rho_b (\rho \beta)_f} Ra Pr (\theta^n + N \Phi^n) - \frac{\Delta \tau \sigma_b \rho_f}{\sigma_f \rho_b} Ha^2 Pr (V^n \cos^2 \gamma - U^n \sin \gamma \cos \gamma) + V^n \quad (26)$$

Step 2:

$$\nabla^2 p^{n+1} = \frac{\rho_b}{\rho_f} \frac{1}{\Delta \tau} \left(\frac{\partial U^*}{\partial X} + \frac{\partial V^*}{\partial Y} \right). \quad (27)$$

Step 3:

$$U^{n+1} = U^* - \Delta \tau \frac{\rho_b}{\rho_f} \left(\frac{\partial P}{\partial X} \right)^{n+1}, \quad (28)$$

$$V^{n+1} = V^* - \Delta \tau \frac{\rho_b}{\rho_f} \left(\frac{\partial P}{\partial Y} \right)^{n+1}. \quad (29)$$

Step 4:

$$\theta^{n+1} = \frac{k_{m,b} \Delta \tau}{k_f} cr \left(\frac{\partial^2 \theta}{\partial X^2} + \frac{\partial^2 \theta}{\partial Y^2} \right)^n + \theta^n, \quad (30)$$

$$\Phi^{n+1} = \frac{\Delta \tau}{Le} \left(\frac{\partial^2 \Phi}{\partial X^2} + \frac{\partial^2 \Phi}{\partial Y^2} \right)^n + \Phi^n, \quad (31)$$

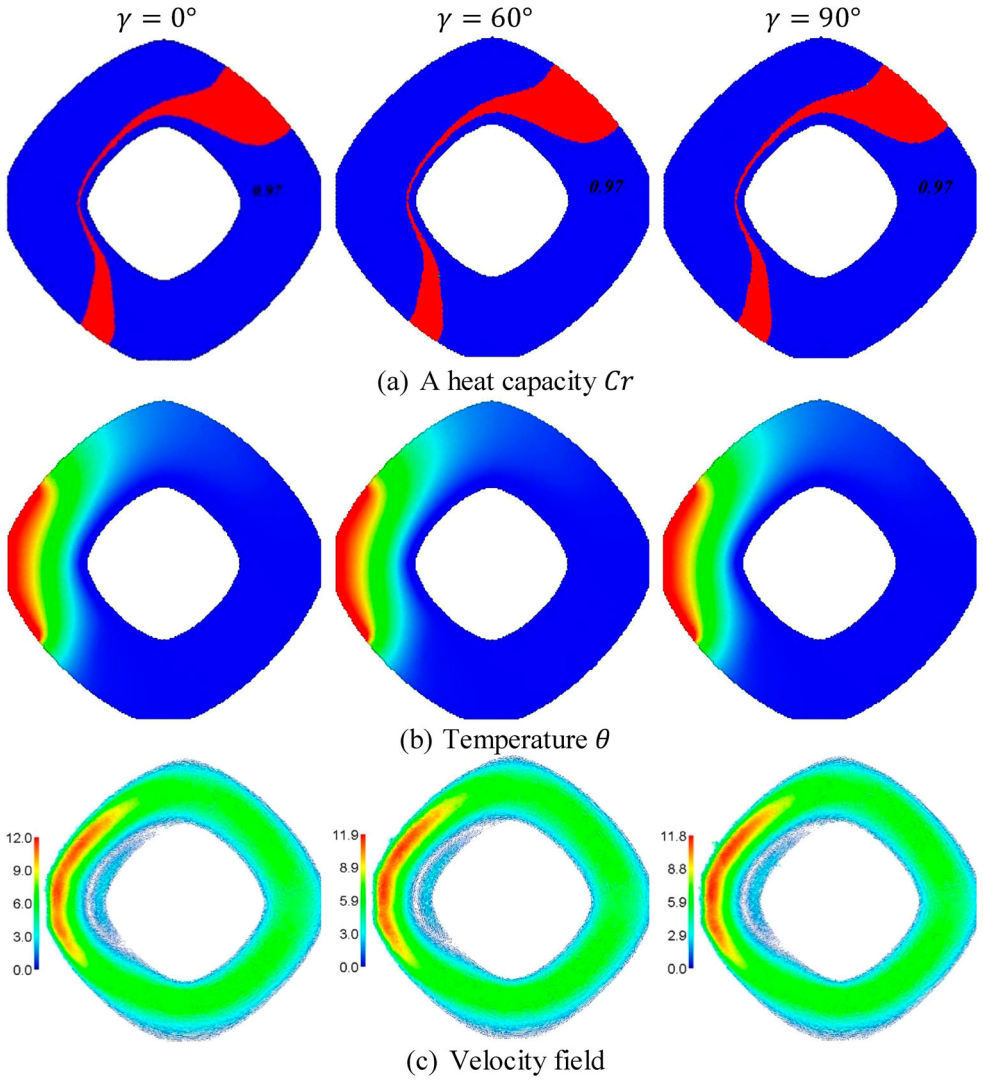


Figure 4. Effects of an inclination angle γ on the regulating fields at $Ha = 20, \varphi = 0.05, \theta_f = 0.05, N = 1, Le = 10, L_x = 0.2, Ra = 10^4$, and $Ste = 0.2$.

Step 5:

$$\mathbf{r}^{n+1} = \Delta \tau \mathbf{U}^{n+1} + \mathbf{r}^n. \quad (32)$$

Shifting technique is:

$$\varphi_{i'} = \varphi_i + (\nabla \varphi)_i \cdot \delta \mathbf{r}_{ii'} + \mathcal{O}(\delta r_{ii'}^2), \quad (33)$$

4. Results and discussion

This section introduces ISPH simulations of suspension of NEPCM within an annulus between two super ellipses under the inspirations of a magnetic field. The fixed

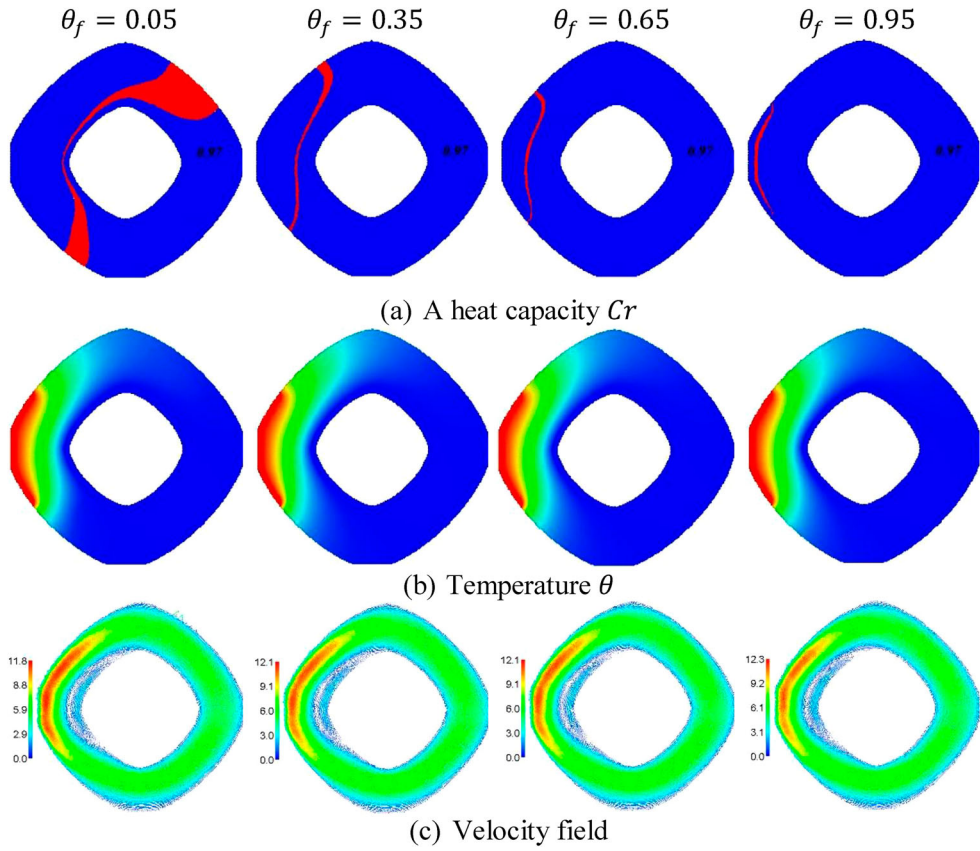


Figure 5. Effects of the fusion temperature parameter on the regulating fields at $\varphi = 0.05$, $Ha = 20$, $N = 1$, $Le = 10$, $L_x = 0.2$, $Ra = 10^4$, and $Ste = 0.2$.

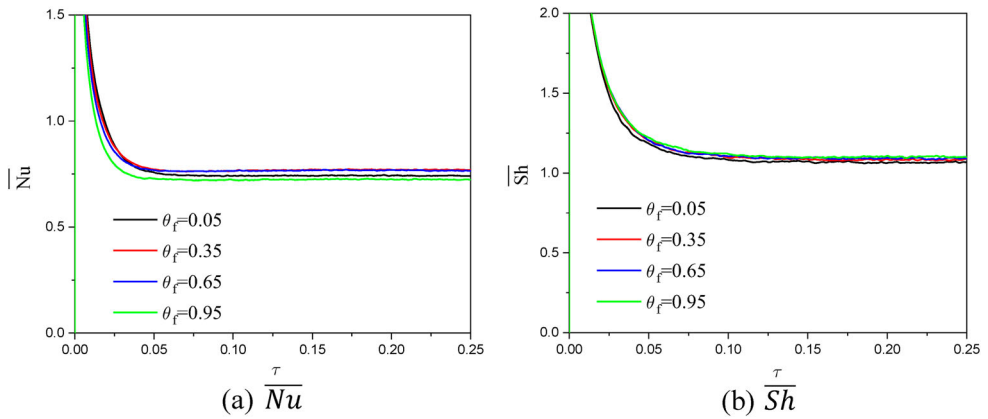


Figure 6. Effects of the fusion temperature parameter on \overline{Nu} and \overline{Sh} at $\varphi = 0.05$, $Ha = 20$, $N = 1$, $Le = 10$, $L_x = 0.2$, $Ra = 10^4$, and $Ste = 0.2$.

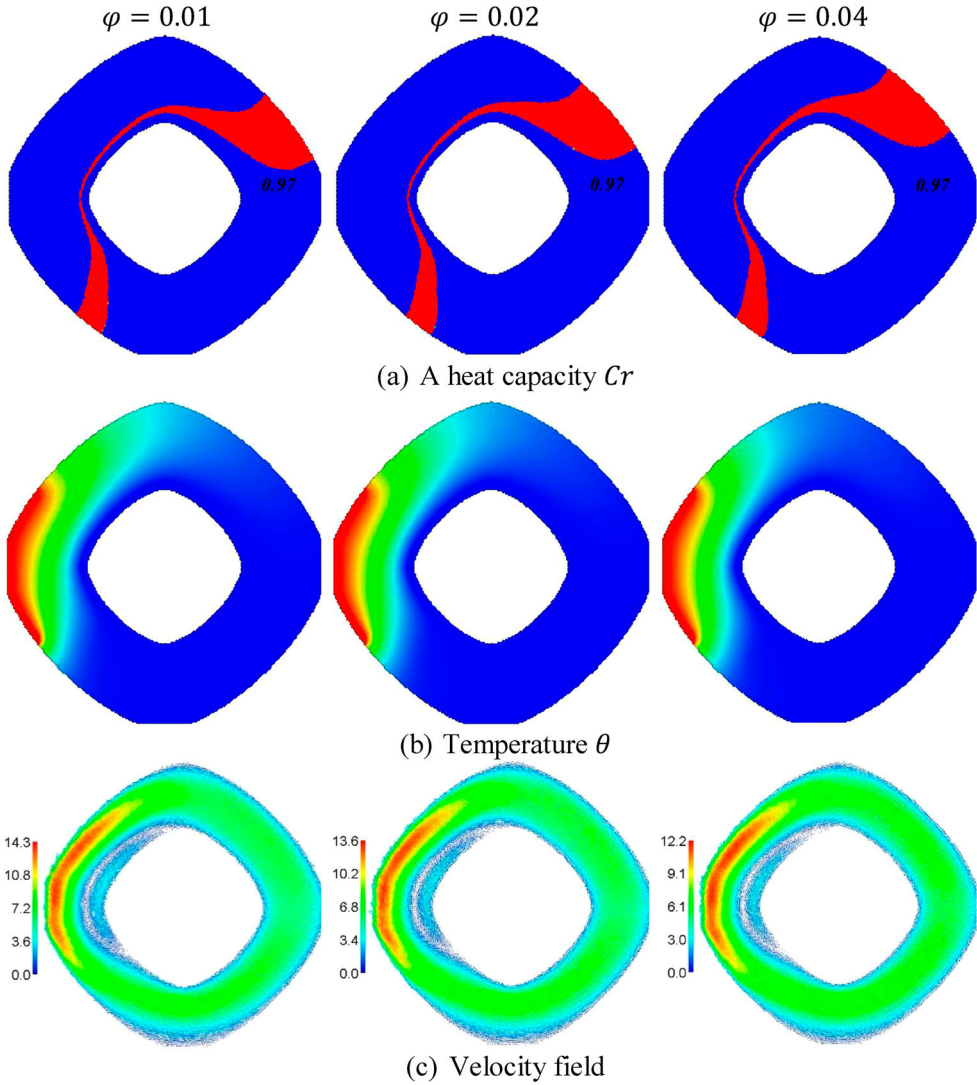


Figure 7. Effects of the solid volume fraction on the regulating fields at $\theta_f = 0.05$, $Ha = 20$, $N = 1$, $Le = 10$, $L_x = 0.2$, $Ra = 10^4$, and $Ste = 0.2$.

parameters are Prandtl number $Pr = 4.623$, and Lewis number $Le = 10$. The physical parameters are scaled as Hartmann number ($Ha = 0 - 40$), an inclination angle of a magnetic field ($\gamma = 0^\circ - 90^\circ$), a fusion temperature ($\theta_f = 0.05 - 0.95$), solid volume fraction ($\varphi = 0.01 - 0.04$), partial heat/mass source ($L_x = 0.1 - 1$), the Stefan parameter ($Ste = 0.1 - 0.8$), Rayleigh number ($Ra = 10^3 - 10^5$), and buoyancy ratio parameter ($N = -2 - 5$).

4.1. The magnetic field parameters

Figures 2 and 3 introduce the reliance of a heat capacity, temperature, concentration, and velocity field as well as the values of \overline{Nu} and \overline{Sh} on the Hartmann number when $\gamma = 30^\circ$, $\varphi =$

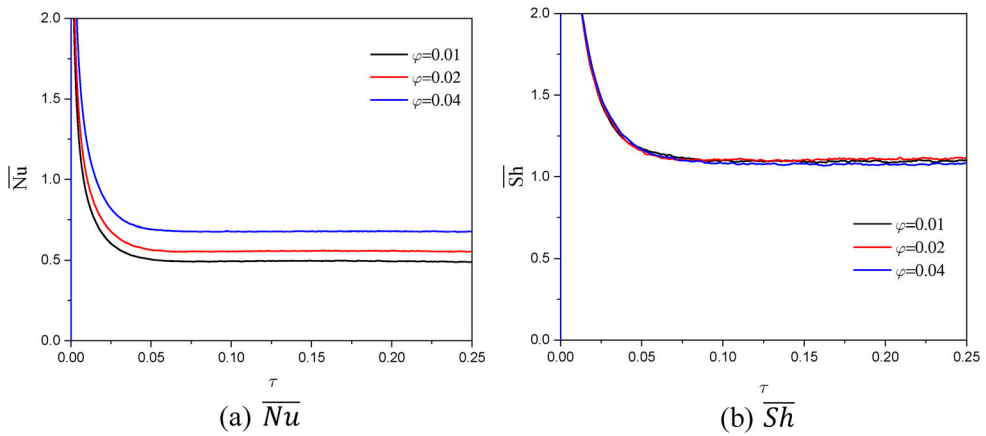


Figure 8. Effects of the solid volume fraction on \overline{Nu} and \overline{Sh} at $\theta_f = 0.05$, $Ha = 20$, $N = 1$, $Le = 10$, $L_x = 0.2$, $Ra = 10^4$, and $Ste = 0.2$.

0.05, $\theta_f = 0.05$, $N = 1$, $Le = 10$, $L_x = 0.2$, $Ra = 10^4$, and $Ste = 0.2$. According to an increase in the Hartmann number, the phase change material (PCM) zone shifts closer to the heater zone in the left area of an annulus. The physical reason for these results returns to the temperature distributions in Figure 2(b). In this figure, the temperature is reducing through the annulus according to an increment in the Hartmann number. Further, the concentration is shrinking into the left area of the annulus as the Hartmann number powers, as shown in Figure 2(c). Physically, the strength in the Lorentz force powers as Ha increases. The Lorentz force minimizes the velocity of the fluid flow. As a result, an increase on Ha from 0 to 40 reduces the maximum of the nanofluid velocity by 73.55%. In Figure 3, the values of \overline{Nu} and \overline{Sh} are decreasing according to an expansion in the Hartmann number.

Figure 4 shows the effects of an inclination angle γ for a magnetic field on the heat capacity, temperature, concentration, and velocity field at $Ha = 20$, $\varphi = 0.05$, $\theta_f = 0.05$, $N = 1$, $Le = 10$, $L_x = 0.2$, $Ra = 10^4$, and $Ste = 0.2$. In Figure 4(a,b), there are minor changes in the PCM zone and temperature distributions below the variations on γ ($\gamma = 0^\circ - 90^\circ$). In Figure 4(c), the velocity's maximum is slightly decreasing by 1.67% as γ increases from 0° to 90° .

4.2. The fusion temperature parameter

Figures 5 and 6 show the influences of a fusion temperature parameter θ_f on the heat capacity, temperature, velocity field, \overline{Nu} , and \overline{Sh} at $\varphi = 0.05$, $Ha = 20$, $N = 1$, $Le = 10$, $L_x = 0.2$, $Ra = 10^4$, and $Ste = 0.2$. In Figure 5(a), according to an increment in the value of θ_f , the intensity of the PCM zone weakens, and the PCM zone shifts nearer to the heater. In a region near the heated wall, the temperature gradients are strong, and thus, the temperature variation and phase transition zone shrink to a narrow physical space. In Figure 5(b), it is remarked that the variations on θ_f are slightly enhance the temperature distributions within an annulus. In Figure 5(c), the velocity's maximum gains around 4.24% as θ_f rises from 0.05 to 0.95. In Figure 6, the values of \overline{Nu} and \overline{Sh} are not significantly affected by changes on θ_f . Thus, it is well mentioned that the fusion temperature parameter has a significant role

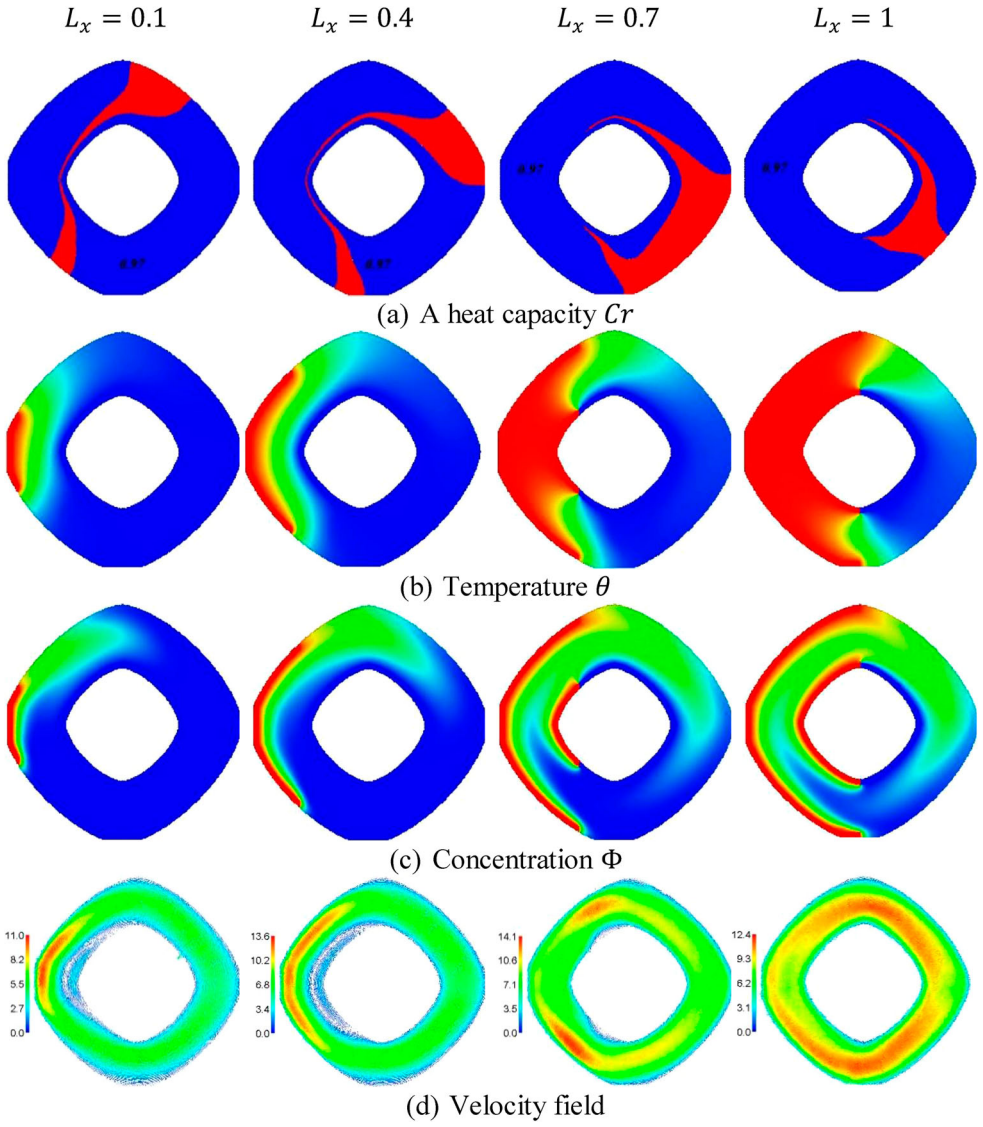


Figure 9. Effects of the Partial heat/mass source length L_x on the regulating fields at $\gamma = 30^\circ$, $\varphi = 0.05$, $\theta_f = 0.05$, $N = 1$, $Le = 10$, $Ha = 20$, $Ra = 10^4$, and $Ste = 0.2$.

in controlling the zone of PCM within an annulus, whilst its contributions in improving the nanofluid motions and transmission of heat and mass within an annulus are minor.

4.3. The nanoparticles parameter

Figures 7 and 8 present the influences of the solid volume fraction φ on the heat capacity, temperature, velocity field, \overline{Nu} , and \overline{Sh} at $\theta_f = 0.05$, $Ha = 20$, $N = 1$, $Le = 10$, $L_x = 0.2$, $Ra = 10^4$, and $Ste = 0.2$. Here, due to the suspension of NEPCM inside an annulus, adding

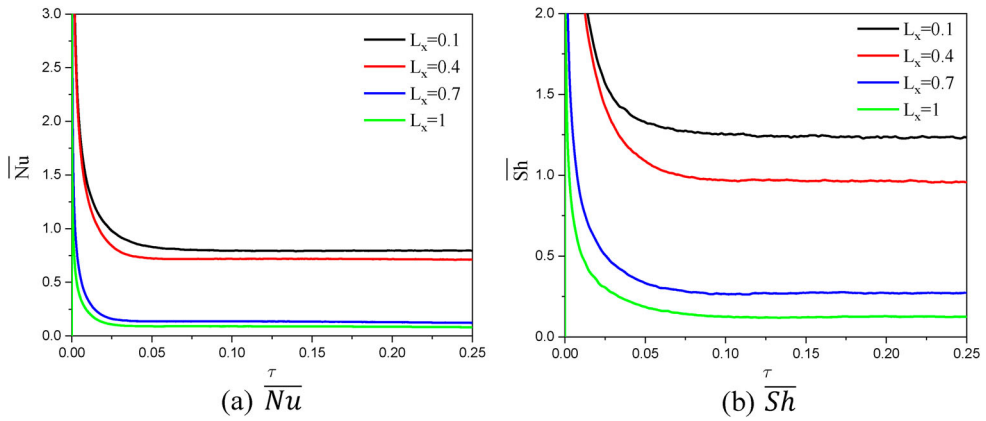


Figure 10. Effects of the Partial heat/mass source length L_x on \overline{Nu} and \overline{Sh} at $\gamma = 30^\circ$, $\varphi = 0.05$, $\theta_f = 0.05$, $N = 1$, $Le = 10$, $Ha = 20$, $Ra = 10^4$, and $Ste = 0.2$.

nanoparticles is limited to 5%. In Figure 7(a), it is noted that the strength of a heat capacity Cr raises as the solid volume fraction increases, and these results are returning to Eq. (23), in which the value of Cr is calculated from the solid volume fraction φ . In Figure 7(b,c), the temperature contours have almost little decrease corresponding to adding the extra concentration of the nanoparticles. Further, the maximum of the velocity field declines by 14.68% as φ increases from 0.01 to 0.04. These results are relevant to the extra viscosity of the mixture-fluid when adding more concentrations of the nanoparticles. In Figure 8, as φ increases, the values of \overline{Nu} is enhanced, and the values of \overline{Sh} are slightly influenced.

4.4. Partial heat/mass source

Figures 9 and 10 show the influences of the partial heat/mass source length L_x on the heat capacity, temperature, concentration, velocity field, \overline{Nu} , and \overline{Sh} at $\gamma = 30^\circ$, $\varphi = 0.05$, $\theta_f = 0.05$, $N = 1$, $Le = 10$, $Ha = 20$, $Ra = 10^4$, and $Ste = 0.2$. The first observation is that an extension in the value of L_x powers the temperature within an annulus, and accordingly, the zone of PCM is shrinking into the right area of the annulus as L_x is expanded. The concentration is distributed within the right area of the annulus according to an increase in L_x . The strength of the velocity field is expanded across the annulus as L_x increases. In Figure 10, an increment on the partial heat/mass source length L_x leads to a clear decrease in the values of \overline{Nu} and \overline{Sh} measured on the heat/mass source.

4.5. A Stefan parameter

Figures 11 and 12 introduce the influences of the Stefan parameter on the heat capacity, temperature, velocity field, \overline{Nu} , and \overline{Sh} at $\gamma = 30^\circ$, $\varphi = 0.05$, $\theta_f = 0.05$, $N = 1$, $Le = 10$, $Ha = 20$, $Ra = 10^4$, and $L_x = 0.2$. In Figure 11, the intensity of the PCM zone is decreasing as a Stefan parameter Ste increases. Further, there are slight changes in the temperature within an annulus according to the variations on Ste . The velocity's maximum increases by 4.31% as Ste increases from 0.1 to 0.8. In Figure 12, as Ste increases, the values of \overline{Nu} are decreasing, and the values of \overline{Sh} are increasing.

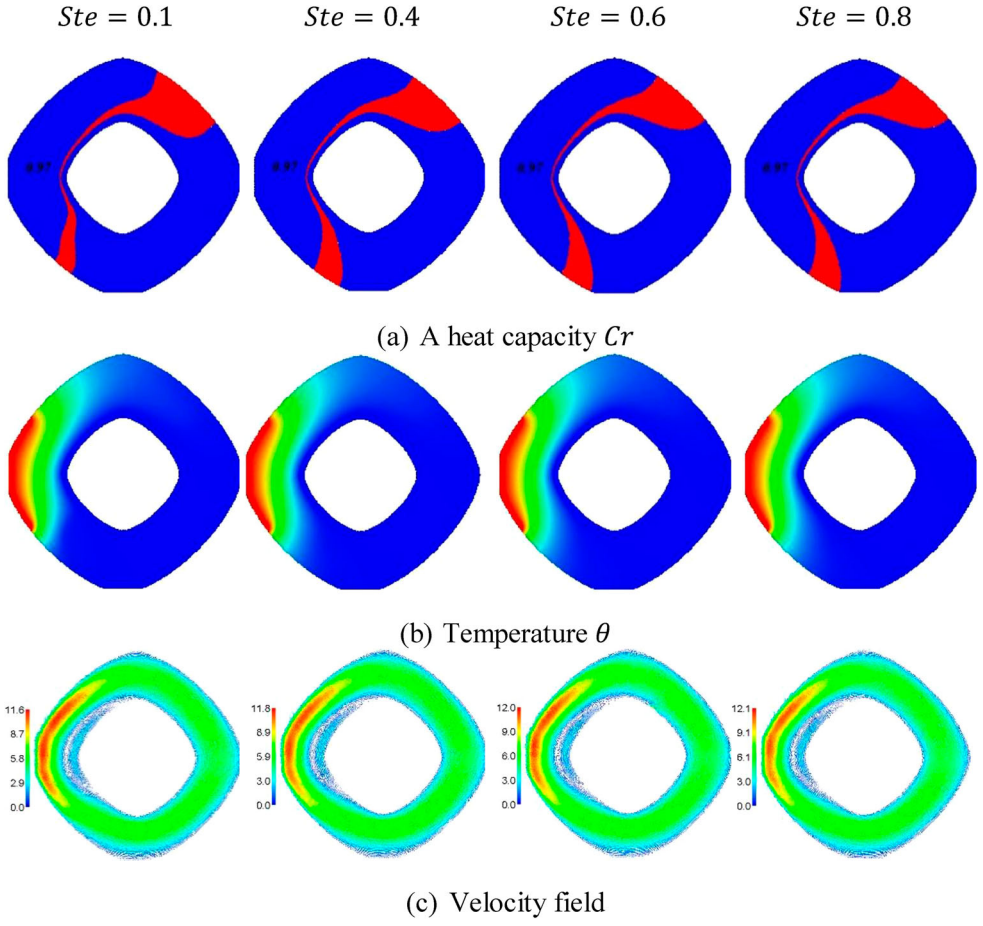


Figure 11. Effects of the Stefan parameter on the regulating fields at $\gamma = 30^\circ$, $\varphi = 0.05$, $\theta_f = 0.05$, $N = 1$, $Le = 10$, $Ha = 20$, $Ra = 10^4$, and $L_x = 0.2$.

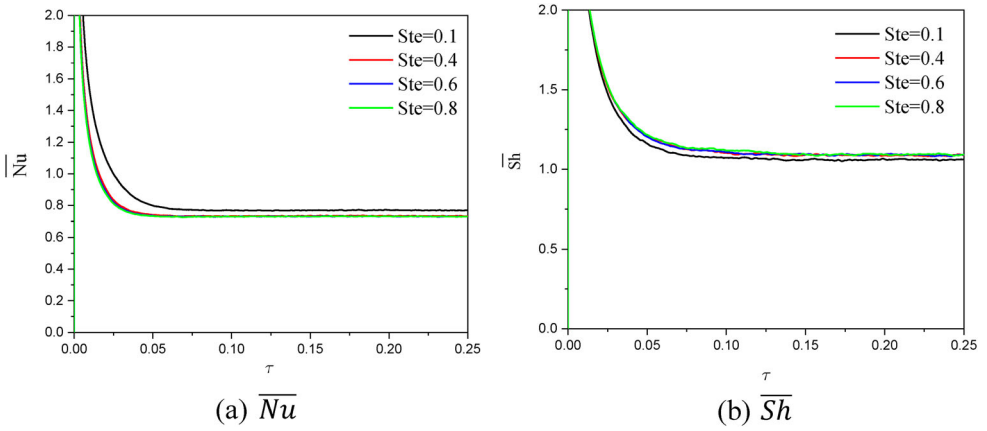


Figure 12. Effects of the Stefan parameter on \overline{Nu} and \overline{Sh} at $\gamma = 30^\circ$, $\varphi = 0.05$, $\theta_f = 0.05$, $N = 1$, $Le = 10$, $Ha = 20$, $Ra = 10^4$, and $L_x = 0.2$.

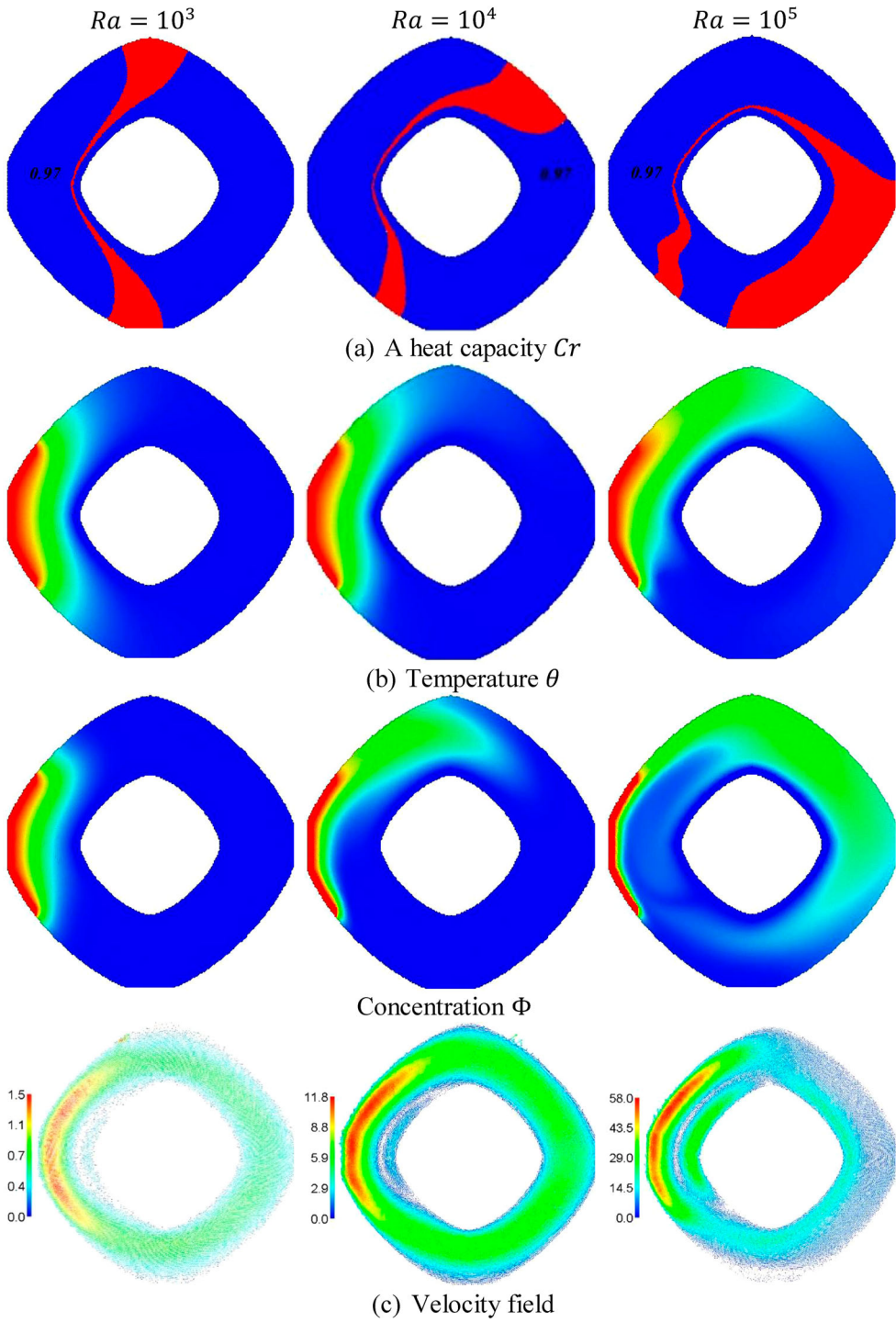


Figure 13. Effects of Rayleigh number on the regulating fields at $\theta_f = 0.05$, $Ha = 20$, $N = 1$, $Le = 10$, $L_x = 0.2$, $\varphi = 0.05$, and $Ste = 0.2$.

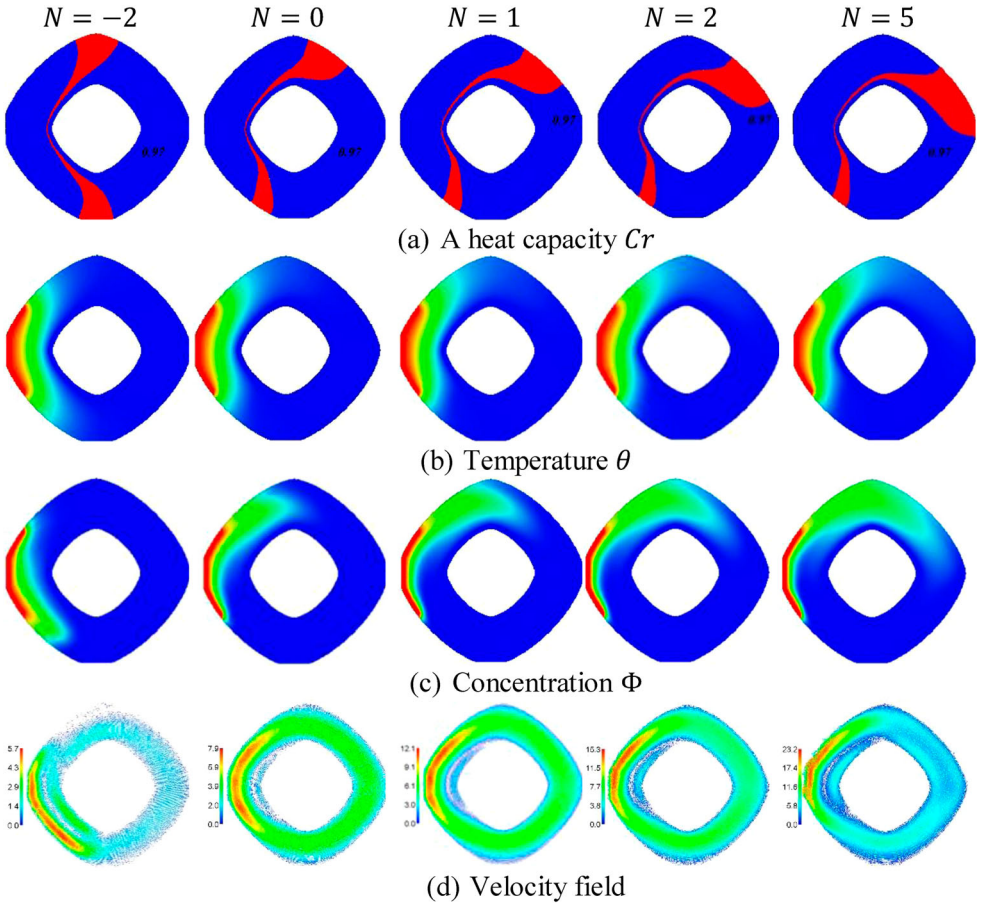


Figure 14. Effects of buoyancy parameter N on the regulating fields at $\gamma = 30^\circ$, $\varphi = 0.05$, $\theta_f = 0.05$, $Le = 10$, $Ste = 0.2$, $Ha = 20$, $Ra = 10^4$, and $L_x = 0.2$.

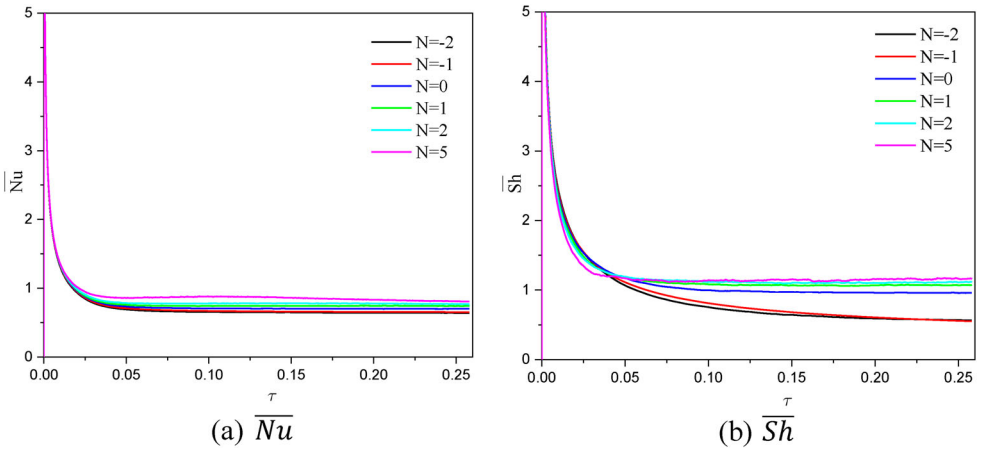


Figure 15. Effects of buoyancy parameter N on \overline{Nu} and \overline{Sh} at $\gamma = 30^\circ$, $Ste = 0.2$, $\varphi = 0.05$, $\theta_f = 0.05$, $Le = 10$, $Ha = 20$, $Ra = 10^4$, and $L_x = 0.2$.

4.6. Rayleigh number

Figure 13 shows the influences of the Rayleigh number on the heat capacity, temperature, concentration, velocity field, \overline{Nu} , and \overline{Sh} at $\theta_f = 0.05$, $Ha = 20$, $N = 1$, $Le = 10$, $L_x = 0.2$, $\varphi = 0.05$, and $Ste = 0.2$. An increment in Ra from 10^3 to 10^5 , the zone of PCM shifts towards the right area of an annulus, and the intensity of PCM zone powers. Further, an increment in Ra powers the buoyancy forces, and so the temperature and concentration distributions are grown through an annulus. Thus, the high buoyancy forces are generating high fluid motions and so the velocity's maximum increases strongly.

4.7. Buoyancy ratio parameter

Figures 14 and 15 indicate the impacts of buoyancy ratio parameter N on the heat capacity, temperature, concentration, velocity field, \overline{Nu} , and \overline{Sh} at $\gamma = 30^\circ$, $\varphi = 0.05$, $\theta_f = 0.05$, $Le = 10$, $Ste = 0.2$, $Ha = 20$, $Ra = 10^4$, and $L_x = 0.2$. Physically, there is two different flow regimes according to the value of N including aiding flow at $N \geq 1$ and opposing flow at $N \leq -1$. As a result, the PCM zone, isotherms and isoconcentration are changing from inwards to upwards according to the changes in N from -2 to positive values $N \geq 1$. Further, the PCM zone increases and shifts upwards according to an increase in N . Besides, the isotherms and isoconcentration are increasing upwards according to an increase in N . Due to higher buoyancy forces at extra N , the nanofluid velocity is dramatically enhanced according to an increase in N . In Figure 15, the values of \overline{Nu} and \overline{Sh} are enhanced as N boosts.

5. Conclusion

Thermosolutal convection of a nanofluid contained NEPCM suspended in the host fluid within an annulus between two super ellipses is discussed numerically by the ISPH method. In a novel annulus shape, the heat/mass source with a variable length is placed on the left side. A numerical scheme based on the ISPH method is utilized to deal with the transformed regulating equations. The conclusive statements for the ISPH simulations are deliberated as:

- Growing the Hartmann number, the PCM transition zone shifts nearly to the heat/mass source, and the temperature, concentration, nanofluid speed, rate of heat, and mass transmission are lowering.
- Increasing θ_f , the intensity of the PCM transition zone weakens, and the PCM zone shifts nearer to the heat/mass source, and velocity's maximum increases by 4.24%.
- Growing solid volume fraction to $\varphi = 0.04$ strengthens the heat capacity Cr and raises the viscosity of the base fluid, so the velocity's maximum reduces by 14.68%.
- The length of heat/mass source L_x is acting as an effective tool in enhancing the transport of heat and mass and nanofluid motions within an annulus.
- The strength of PCM powers and the nanofluid speed is strongly growing as the Rayleigh number increases.
- Increasing buoyancy ratio parameter augments the PCM transition zone, isotherms, isoconcentration and velocity field due to extra buoyancy forces within an annulus.

Acknowledgements

The authors extend their appreciation to the Deanship of Scientific Research at King Khalid University, Abha, Saudi Arabia, for funding this work through the Research Group Project under Grant Number (RGP. 1/254/42).

Disclosure statement

No potential conflict of interest was reported by the author(s).

ORCID

Abdelraheem M. Aly  <http://orcid.org/0000-0003-3369-8452>

Zehba Raizah  <http://orcid.org/0000-0002-6529-8050>

Mohammad Ghalambaz  <http://orcid.org/0000-0003-0965-2358>

References

- [1] Hashemi-Tilehnoee M, Dogonchi AS, Seyyedi SM, et al. Magneto-fluid dynamic and second law analysis in a hot porous cavity filled by nanofluid and nano-encapsulated phase change material suspension with different layout of cooling channels. *J Ener Stor*. 2020;31:101720.
- [2] Raizah Z, Aly AM. Double-diffusive convection of a rotating circular cylinder in a porous cavity suspended by nano-encapsulated phase change materials. *Case Stud Therm Eng*. 2021; 100864.
- [3] Chananipoor A, Azizi Z, Raei B, et al. Optimization of the thermal performance of nano-encapsulated phase change material slurry in double pipe heat exchanger: design of experiments using response surface methodology (RSM). *J Build Eng*. 2021;34:101929.
- [4] Hamid M, Usman M, Khan ZH, et al. Heat transfer and flow analysis of Casson fluid enclosed in a partially heated trapezoidal cavity. *Inter Commun Heat Mass Transf*. 2019;108:104284.
- [5] Khan ZH, Makinde OD, Hamid M, et al. Hydromagnetic flow of ferrofluid in an enclosed partially heated trapezoidal cavity filled with a porous medium. *J Magnet Magn Mater*. 2020;499:166241.
- [6] Cho C-C. Effects of porous medium and wavy surface on heat transfer and entropy generation of Cu-water nanofluid natural convection in square cavity containing partially-heated surface. *Inter Commun Heat Mass Transf*. 2020;119:104925.
- [7] Haq RU, Soomro FA, Wang X, et al. Partially heated lid-driven flow in a hexagonal cavity with inner circular obstacle via FEM. *Inter Commun Heat Mass Transf*. 2020;117:104732.
- [8] Nie C, Deng S, Guo H, et al. Effects of partially thermally active walls on simultaneous charging and discharging of paraffin wax in a square cavity. *Ener Convers Manag*. 2019;202:112201.
- [9] Aneja M, Chandra A, Sharma S. Natural convection in a partially heated porous cavity to Casson fluid. *Inter Commun Heat Mass Transf*. 2020;114:104555.
- [10] Abu-Hamdeh NH, Oztop HF, Alnefaie KA. A computational study on mixed convection in a porous media filled and partially heated lid-driven cavity with an open side. *Alexandria Eng J*. 2020;59(3):1735–1750.
- [11] Aly AM. Double-diffusive natural convection in an enclosure including/excluding sloshing rod using a stabilized ISPH method. *Inter Commun Heat Mass Transf*. 2016;73:84–99.
- [12] Aly AM, Ahmed SE, Raizah Z. Double-diffusive natural convection in a square porous cavity with sinusoidal distributions side walls filled with a nanofluid. *J Porous Media*. 2018;21(2):101–122.
- [13] Aly AM, Raizah Z. Double-diffusive convection of solid particles in a porous X-shaped cavity filled with a nanofluid. *Phys Scrip*. 2020;96(1):015301.
- [14] Hu J-T, Mei S-J. Unsteady double diffusive convection inside a partial porous building enclosure subjected to time-periodic temperature boundary condition. *Inter Commun Heat Mass Transf*. 2021;122:105128.
- [15] Srinivasacharya D, Ramana KS. Thermal radiation and double diffusive effects on bioconvection flow of a nanofluid past an inclined wavy surface. *Therm Sci Eng Progr*. 2021;22:100830.

- [16] Moolya S, Satheesh A. Role of magnetic field and cavity inclination on double diffusive mixed convection in rectangular enclosed domain. *Inter Commun Heat Mass Transf.* [2020](#);118:104814.
- [17] Hussain S, Öztıp HF, Qureshi MA, et al. Double diffusive buoyancy induced convection in step-wise open porous cavities filled nanofluid. *Inter Commun Heat Mass Transf.* [2020](#);119:104949.
- [18] Raizah ZA, Aly AM, Ahmed SE. Natural convection flow of a nanofluid-filled V-shaped cavity saturated with a heterogeneous porous medium: incompressible smoothed particle hydrodynamics analysis. *Ain Shams Eng J.* [2021](#);12(2):2033–2046.
- [19] Aly AM. Mixing between solid and fluid particles during natural convection flow of a nanofluid-filled H-shaped cavity with three center gates using ISPH method. *Inter Commun Heat Mass Transf.* [2020](#);157:119803.
- [20] Keramat F, Azari A, Rahideh H, et al. A CFD parametric analysis of natural convection in an H-shaped cavity with two-sided inclined porous fins. *J Taiwan Inst Chem Eng.* [2020](#);114:142–152.
- [21] Ahmed SE, Mansour MA, Alwatban AM, et al. Finite element simulation for MHD ferro-convective flow in an inclined double-lid driven L-shaped enclosure with heated corners. *Alexandria Eng J.* [2020](#);59(1):217–226.
- [22] Bhopalam SR, Perumal DA. Numerical analysis of fluid flows in L-shaped cavities using Lattice Boltzmann method. *Applic Eng Sci.* [2020](#);3:100016.
- [23] Alapati S. Simulation of natural convection in a concentric hexagonal annulus using the Lattice Boltzmann method combined with the smoothed profile method. *Mathematics.* [2020](#);8(6):1043.
- [24] Ali MM, Alim MA, Ahmed SS. Magnetohydrodynamic mixed convection flow in a hexagonal enclosure. *Proc Eng.* [2017](#);194:479–486.
- [25] Rizwan ul H, Soomro FA, Hammouch Z. Heat transfer analysis of CuO-water enclosed in a partially heated rhombus with heated square obstacle. *Inter Commun Heat Mass Transf.* [2018](#);118:773–784.
- [26] Hosseini AA, Nikfar M. Numerical analysis of unsteady natural convection from two heated cylinders inside a rhombus enclosure filled with Cu-water nanofluid. *Inter Commun Heat Mass Transf.* [2020](#);113:104510.
- [27] Ghalambaz M, Mehryan SAM, Zahmatkesh I, et al. Free convection heat transfer analysis of a suspension of nano-encapsulated phase change materials (NEPCMs) in an inclined porous cavity. *Inter J Therm Sci.* [2020](#);157:106503.